Characterizing ultrasonic standing wave fields by schlieren imaging

Wörtche, Frederike S.L.; Maucher, Fabian; Mooiweer, Martijn; Verbiest, Gerard J.; Steeneken, Peter G.

DOI
10.1016/j.ultras.2025.107743

Publication date
2025

Document Version
Final published version

Published in
Ultrasonics

Ultrasonics 156 (2025) 107743

Contents lists available at ScienceDirect

Ultrasonics

journal homepage: www.elsevier.com/locate/ultras

Characterizing ultrasonic standing wave fields by schlieren imaging

Frederike S.L. Wörtche *, Fabian Maucher, Martijn Mooiweer, Gerard J. Verbiest, Peter G. Steeneken *

Department of Precision and Microsystems Engineering, Delft University of Technology, Mekelweg 2, 2628 CD, Delft, The Netherlands

ARTICLE INFO

Keywords:
Acousto-optics
Acoustic levitation
Schlieren
Ultrasonic phased arrays
Standing waves

ABSTRACT

Schlieren imaging is a widely applied optical technique for visualizing small refractive index changes in transparent media. An emerging application of schlieren is real-time monitoring and optimization of ultrasound pressure fields for acoustic levitation applications. However, the typically nonlinear relationship between the schlieren intensity and the pressure field complicates deducing the latter from the former. Here, we propose a method to remove this nonlinear relationship, thereby permitting a more quantitative analysis of the pressure variations in the levitation field. By exploiting the harmonic nature of the pressure field using phase-shifted stroboscopic schlieren images we extract the linear part of the schlieren intensity. This linear part is proportional to the instantaneous pressure gradient. The method is successfully employed experimentally and validated by comparing it to simulated acoustic levitation fields. Thereby, our work paves the way towards an improved quantitative analysis of periodic schlieren images that is easily implemented and is particularly suitable for the analysis of ultrasound pressure fields for acoustic levitation applications.

1. Introduction

Already in the 19th century the idea that matter can be trapped and moved via acoustic waves has captivated scientists [1]. During the last decades, acoustic control over ultrasonic pressure fields has improved tremendously and enabled independently translating and levitating objects within a 3D volume [2–7]. Since it imposes nearly no limitations – apart from weight-restrictions – on material properties for successful lifting, acoustic levitation offers significant advantages over other levitation techniques [8,9]. Consequently, it has been proposed and adapted for a variety of applications, including containerless processing [10–12], volumetric displays [13,14], omnidirectional microscopy [15] and (micro-) assembly processes [9,16].

With the advances of acoustic levitation based applications arises a growing need for accurately and rapidly measuring the ultrasound fields hosting the levitation traps. A straightforward procedure to achieve this is scanning the field using a microphone [17]. However, this method is not ideal since the microphone interacts with the acoustic field and the point-wise measuring of the 3D acoustic grid is time-consuming. Furthermore, the resolution is limited by the microphone size. Optical methods have been found to be a suitable alternative to the microphone due to their non-invasive nature. Interferometric techniques – such as laser Doppler vibrometry – allowed for the accurate reconstruction of the 3D ultrasound field [18]. Yet, the imaging occurs on a pixel-to-pixel basis as a single laser beam has to scan the full 3D field.

A wide-field alternative is measuring the ultrasound fields using schlieren imaging. In a schlieren imaging setup local pressure variations in the levitation field lead to small refractive index gradients. These lead to a weakly modulated phase of the light, which in the geometric optics picture gives rise to a slight deflection of light rays. Partly blocking the light in the focal plane permits admixing the otherwise small phase-variations to the amplitude at the screen. Hence, measuring the light intensity after traversing the levitator with a conventional camera allows real-time observation of the ultrasound field. Due to its simplicity and speed, the schlieren method has recently increasingly been employed for the qualitative analysis of ultrasound fields [19–21] and for optimizing the levitator design [22,23]. Furthermore, the instantaneous mapping permits the simultaneous observation of the field and the levitated particle, granting further insights such as the effect of particle shape on levitation characteristics [24,25].

The difficulty of schlieren imaging lies in the accurate interpretation of the relation between the measured optical intensity and the ultrasound pressure values. This restricts most schlieren observations of levitation fields to only hold qualitative information. Both the calibration of the schlieren system, and the distinction between schlieren contributions related to the pressure gradient and other intensity contributions, present challenges to be overcome before quantitative information on

* Corresponding authors.
E-mail addresses: F.S.L.Wortche@tudelft.nl (F.S.L. Wörtche), P.G.Steeneken@tudelft.nl (P.G. Steeneken).

https://doi.org/10.1016/j.ultras.2025.107743
Received 4 April 2025; Received in revised form 4 June 2025; Accepted 22 June 2025
Available online 4 July 2025

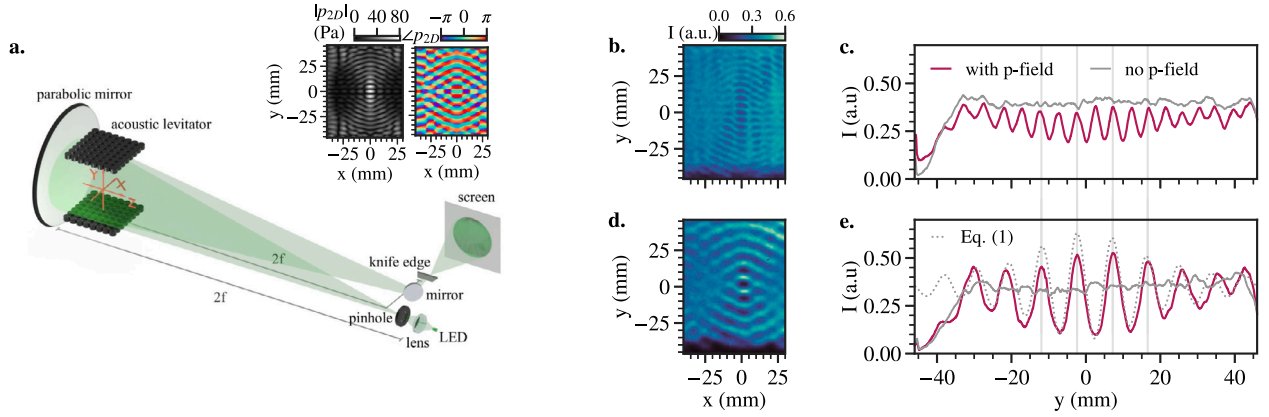

Fig. 1. The schlieren system and its illumination methods. (a.) The schematic overview of the schlieren system (not to scale for convenience of presentation) and the amplitude and phase of the modeled input field p_{2D}. (b.) The observed schlieren image of an acoustic field with a focal point in $\mathbf{r} = (0,0,0)$ ($p_{theo,max} \approx 3.4\,\mathrm{kPa}$) when driving the LED with a continuous signal. A line-cut through $x = 0\,\mathrm{mm}$ of the image (pink) and when no pressure field is present (gray) i.e. the background illumination, is shown in (c.). (d.) Schlieren image of the acoustic field with focal point in $\mathbf{r} = (0,0,0)$ ($p_{theo,max} \approx 1.4\,\mathrm{kPa}$) for a pulsed LED signal. (e.) Line-cuts for $x = 0\,\mathrm{mm}$ of the stroboscopic schlieren image (pink) and when no pressure field is present (gray). When using this LED setting, the obtained schlieren image line-cut displays similarities to the theoretically estimated intensity (dotted line).

the pressure field can be obtained from the schlieren data. For the first requisite, typically a known refractive index gradient is measured to obtain the calibration factor for the system, an example of which being the thin lens method [26]. The second requirement presumes a good understanding of the impact of the acoustic field on the light field to distinguish between the intensity variations depending linearly on the gradient of the ultrasound pressure field and intensity contributions originating from other, potentially nonlinear, sources. It is commonly assumed that there is only a linear relationship between the measured intensity and the pressure gradient [26]. We will show that nonlinear contributions can play an important role.

In this article, we provide a methodology for estimating ultrasound pressure gradients from schlieren images that works in the presence of nonlinear contributions to the schlieren image. We will provide experimental data on standing-wave fields, generated by ultrasound transducer arrays for acoustic levitation, indicating that, in addition to linear contributions, higher order (i.e. nonlinear) intensity variations can be distinguished in schlieren images of these standing-wave based acoustic levitation fields. As a consequence of these nonlinear contributions, the identification of the schlieren signal ascribable to the pressure field gradient becomes more complicated. We propose that the schlieren intensity can be separated in a linear and nonlinear component by exploiting their individual temporal behavior. By applying this separation method to our experimental schlieren images, we can extract the linear intensity component and use it to successfully reconstruct the pressure gradient of the ultrasound field. By comparing this reconstructed pressure gradient to the simulated pressure field we obtain a good agreement, providing evidence for the validity of the methodology.

2. Schlieren intensity

The schlieren system used in this article is a single mirror system; a pinhole with radius $R = 75\,\mu\mathrm{m}$ and a knife-edge, parallel to the x-axis, are placed at twice the focal distance $2f$=4.064 m of a parabolic mirror, see Fig. 1(a). An image of the pinhole is projected on the knife-edge plane. The knife-edge then blocks the light within roughly a half-space [26,27]. The acoustic levitator consists of two ultrasound transducer arrays which generate spatiotemporal pressure variations $p(x,y,z,t)$ that slightly modulate the refractive index of air: $n(x,y,z,t) \approx 1 + \kappa p(x,y,z,t)$. The constant κ corresponds to $\kappa \approx 2.7 \times 10^{-9}\ \mathrm{Pa}^{-1}$ for visible light in air at atmospheric pressure at room temperature [26, 28]. We consider a light beam that propagates through the schlieren setup (Fig. 1(a)) and traverses the pressure field approximately parallel to the optical axis in the z-direction. The inset plots of Fig. 1(a) depict the amplitude and phase of an averaged pressure field $p_{2D}(x,y)$ that was obtained by averaging the original pressure field $p(x,y,z)$ along the z-direction over the length L of the pressure field, i.e. $p_{2D}(x,y,t) = \frac{1}{L}\int_0^L p(x,y,z',t)dz'$. The pressure field in the figure was generated by configuring all transducers in the arrays such that they constructively interfere at an acoustic focal point at position r=(0,0,0), thus creating a locally confined high pressure amplitude.

Upon passing through the spatially modulated pressure field, the light will acquire an additional phase shift $\varphi(x,y,t) = 2k_0 L\kappa p_{2D}(x,y,t)$. Here, $k_0 = 2\pi/\lambda_l$ is the wave number of the light, and the factor two is due to the light passing twice through the pressure field (cf. Fig. 1(a)). We assumed that the change in refractive index is sufficiently small, such that we can use the integrated field along the z-direction to obtain the cumulative effect. Without going further into the details of how the schlieren system transforms phase modulations $\varphi(x,y)$ to intensity modulations, it can generally be stated that the three-dimensional pressure field $p(x,y,z,t)$ will be mapped to a two-dimensional light intensity distribution $I(x_s,y_s,t)$ on a screen with coordinates (x_s,y_s). This projection can be described by an instantaneous mapping $\mathcal{F}$: $p_{2D}(x,y) \to I(x_s,y_s)$.

It is known from schlieren theory [26] that, for sufficiently small pressure variations, there is a linear relation between the intensity and the y-component of the pressure gradient (perpendicular to the knife-edge) which can be approximated as

$$I(x_s,y_s,t) \approx I_0(x_s,y_s)\left[1 + c_1 2L\partial_y p_{2D}\left(\frac{x_s}{m},\frac{y_s}{m},t\right)\right] + \mathcal{O}(p_{2D}^2) \tag{1}$$

where m is the optical magnification of the projected pressure field on the screen, and c_1 is a linear factor that relates pressure gradients to intensity variations. Without loss of generality, for the rest of this paper we will assume that we work with a magnification $m = 1$ to simplify the analysis, such that $I(x_s,y_s,t) = I(x,y,t)$.

A key question with respect to the interpretation of schlieren images is whether the higher order terms $\mathcal{O}(p_{2D}^2)$ in Eq. (1) can be neglected. This question can be answered by evaluating the time-averaged intensity $\langle I(x_s,y_s,t)\rangle_t$. For a harmonically oscillating pressure field $p_{2D}(x,y,t) = p_{2D}(x,y)\cos(\omega t)$ (i.e. a standing wave), the time average of the pressure dependent term should be zero in the absence of higher order terms. Yet, schlieren measurements of the acoustic focal point under continuous illumination in Fig. 1(b), (c) clearly show an intensity modulation. In the absence of the acoustic field this modulation fully disappears (gray curve in Fig. 1(c)), suggesting that this modulation is not due to the pressure independent background $I_0(x_s,y_s)$. We furthermore note that the wavelength of the modulation

is halved compared to the pressure field wavelength ($\lambda = 8.6\,\mathrm{mm}$) which makes it reasonable to assume that the intensity modulation is caused by the higher order term $\mathcal{O}(p_{2D}^2)$.

For comparison, we show in Fig. 1(d), (e) the schlieren image for stroboscopic illumination operated at the transducer frequency ω, such that the acoustic field is probed at a specific moment of its oscillation cycle. Probing the same acoustic field containing the focal point, it appears that the modulation amplitude is roughly twice as large and the wavelength of the intensity modulation matches the pressure field wavelength.

The dotted line in Fig. 1(e) also shows a theoretical estimate of the schlieren intensity based on Eq. (1) (excluding $\mathcal{O}(p_{2D}^2)$ terms) where I_0 has been determined from the gray curve, the pressure field is modeled as given in Section 3.3 and c_1 is chosen such that the minimum of the measured and theoretical intensity coincide. While the general behavior is reasonably described by the linear approximation, the positive amplitudes of the experiment and theory show an apparent discrepancy. Based on the observations in Fig. 1(b)–(e) it has become clear that the higher order terms $\mathcal{O}(p_{2D}^2)$ can impact the schlieren image.

From the measurements in Fig. 1, we can thus deduce that the mapping function $\mathcal{F}$ requires a nonlinear dependency on p_{2D} such that the time averaged intensity will not reduce to zero. In general, given that we consider a harmonic pressure field ($p_{2D}(x,y)\cos(\omega t)$), it makes sense to expand the intensity variation (I_h) as a Fourier-series to acquire the time-dependency of the schlieren intensity,

$$\begin{aligned} I(x,y,t) &= I_0(x,y) + I_h(x,y,t) \\ &= I_0(x,y) + a_0 + a_1\cos(\omega t) + a_2\cos(2\omega t) + \cdots \end{aligned} \tag{2}$$

where I_0 is the pressure independent background of our schlieren system and $a_n = a_n(x,y)$ with $n = 0, 1, 2, \ldots$ are the Fourier coefficients. It follows from Eq. (2), as outlined in more detail in supplemental Sec. 1, that we obtain the following expression for the schlieren intensity,

$$I(x,y,t) \approx I_0(x,y) + I_1(x,y)\cos(\omega t) + I_2(x,y)\cos^2(\omega t) + \ldots. \tag{3}$$

Here, according to Eq. (1), $I_1(x,y) \approx c_1 2L I_0(x,y)\partial_y p_{2D}(x,y)$ and I_2 represents second-order contributions of the pressure. We neglect all other contributions I_n corresponding to Fourier coefficients with $n \geq 3$. This expression for the intensity appears not only formally reasonable, but also in light of the experimental observation presented in Fig. 1(b)–(e).

Note that in the case of continuous illumination, as shown in Fig. 1(c), the modulations in the measured intensity can be explained by the presence of the term $I_2(x,y)$, because $\langle I(x,y)\rangle_t - I_0(x,y) = \frac{1}{2}I_2(x,y)$. The nonlinearities in the schlieren system that give rise to I_2 are rather complex and their discussion is out of the scope of this article. Instead, in this work we propose a method to separate out the I_1 terms in Eq. (3) to facilitate more quantitative analysis of the schlieren images, as will be addressed in the following.

3. Implementation of phase-shifted stroboscopic schlieren technique

In this section, we discuss a proposed methodology to isolate the linear intensity contribution I_1 from the other terms in Eq. (3), which can then be used to estimate the pressure gradient using $I_1(x,y) = c_1 2L I_0(x,y)\partial_y p_{2D}(x,y)$. First, the method and its practical implementation in our schlieren imaging setup is presented. After that, the model used for estimating the pressure field of the acoustic levitator is described.

3.1. Extracting I_1 by phase-shifted strobing

For a schlieren intensity that obeys Eq. (3), it follows that the linear intensity contribution $I_1(x,y)$ can be extracted using the relation:

$$I\left(x,y,t_1\right) - I\left(x,y,t_1 + \frac{\pi}{\omega}\right) = 2I_1(x,y,t=t_1). \tag{4}$$

Thus, in order to extract the linear schlieren contribution I_1 it suffices to measure the intensity at two times (t_1 and $t_1 + T/2 = t_1 + \pi/\omega$, with T denoting the period). This permits establishing a simple relationship of the measured intensity and the pressure gradient at a given time t_1. We can experimentally realize the measurement at the two moments t_1 and $t_1 + T/2$, corresponding to acoustic field phases that are phase shifted by π, using stroboscopic illumination at angular frequency ω equal to that of the generated ultrasound field. The LED strobe time t_1 is chosen to coincide with the moment at which I_1 and the pressure at the trap are maximal, and define our timescale such that $t_1 = 0$ in Eq. (4). Therefore, Eq. (4) is the core of the proposed methodology for extracting I_1 by phase-shifted stroboscopic schlieren measurements.

We note that with this stroboscopic approach, higher-order odd terms such as $I_{3,5,\ldots}$ in Eq. (3), might result in parasitic contributions to the extracted I_1. If needed, a lock-in technique, where the light intensity is harmonically modulated at ω, might be used to filter out these small higher-order contributions. In our experiments we found that these higher-order contributions could not be resolved within our experimental resolution. Therefore, we have employed the stroboscopic approach for its simplicity.

3.2. Schlieren imaging setup

A general overview of the setup used for generating the stroboscopic schlieren images is shown in Fig. 1(a); we create a physical point-like source by placing a pinhole (Thorlabs, P150K) with a diameter of $d = 150\,\mu\mathrm{m}$ in front of a conventional 5 mm green light emitting diode (LED) (NSPG500DS-G, $\lambda_l \approx 532\,\mathrm{nm}$). To enhance the intensity of the pinhole output, the emitted light from the LED is collected by a condenser lens (Thorlabs, AC254-030-AB $d = 1\varepsilon, f_c = 30\,\mathrm{mm}$) and focused onto the pinhole with a magnification close to -1. The pinhole is placed at a distance $2f$ from a parabolic mirror (Edmund optics, d = 8″, $f = 2032\,\mathrm{mm}$, enhanced aluminium) under a slight angle such that the reflected light is directed via a 45° rotated mirror onto a commercial razor blade, which serves as the knife-edge. To allow precise tuning of the intensity cutoff, the razor blade is mounted onto a manual translation stage that can be read out with 10 μm step resolution along the three spatial axes (three stacked Thorlabs PT1/M stages). The distance between parabolic mirror and the knife edge is adjusted such that the point source is focused onto the knife-edge.

Behind the knife-edge we placed a camera (Fujifilm X-T5, positioned at the location of the white screen in Fig. 1(a)) with hyper-zoom telelens (Sigma 60-600 mm 1:4.5-6.3 DG) to capture the schlieren images. The levitator itself is placed close to the parabolic mirror (≈ 5 cm edge-to-edge distance), ensuring high imaging resolution.

To enable stroboscopic illumination, the LED is driven with a pulsed signal triggered by the waveform that drives the transducers, at a frequency of 39.8 kHz. To acquire the schlieren images, we adjust the camera's focal distance so that the central levitator plane is in focus. To minimize acquisition of artifacts due to noise and parasitic effects, such as those caused by transducer heating or ambient air-flow, we record movies of the acoustic field for $\sim 8-14$ seconds and average the intensity of the frames to obtain an averaged schlieren image. During these recordings, we set the frame rate to 30 fps, the shutter speed to 1/30 s, the f-stop to $f/4.5$, and the ISO value to 1000. Since the LED used in our setup emits green light, we exclusively employ the green channel of our images for the analysis.

We note that although we assume the light rays to traverse the pressure field as parallel rays, the off-centered rays actually pass under a slight angle. This angle δ can be estimated from the height of the pressure field ($H_p = 92\,\mathrm{mm}$) and its distance to the pinhole ($2f \sim 4$ m) to be less than $\delta < \arctan H_p/(4f) = 0.7°$, which suggests that the parallel ray approximation is quite reasonable and that the effect of this angle on the schlieren image will be limited. Since we use an off-axis schlieren setup, there is also a small angle between light incident and reflected from the mirror, which we estimate to be ≈ 0.3°.

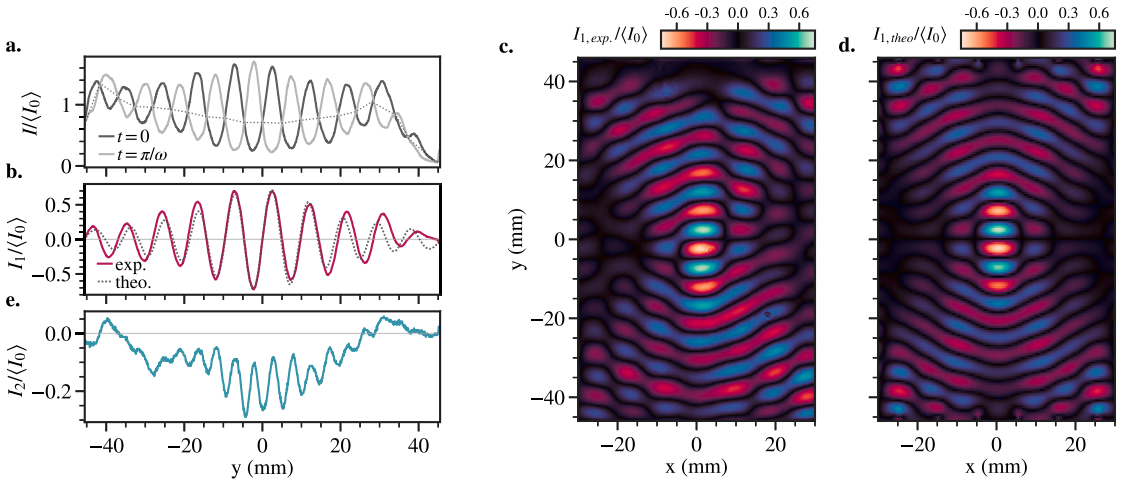

Fig. 2. The phase-shifted stroboscopic schlieren analysis method to estimate the pressure gradient $\partial_y p_{2D}$ from the schlieren intensity. (a.) Line-cuts at $x = 0\,\text{mm}$ of the stroboscopic schlieren images of a focal point for temporal phases $\omega t = 0$ (black) and $\omega t = \pi$ (gray) normalized to the average background intensity $\langle I_0\rangle$. The dotted line interpolates the crossing points of the two measured curves, i.e. where $I(t = 0) = I(t = \pi/\omega)$ (b.) The normalized linearized schlieren intensity $I_1(y)/\langle I_0\rangle$ at $x = 0\,\text{mm}$ and t = 0 extracted from the intensity line-cuts shown in (a) (exp) compared to the modeled intensity (theo). The modeled intensity is obtained using $I_{1,\text{theo}}(x, y, t = 0)/\langle I_0\rangle = c_1 2L\partial_y p_{2D}(x, y, t = 0)$ where the integrated pressure field p_{2D} is acquired as described in Section 3.3. (c., d.) The 2D images of the experimentally obtained $I_{1,\text{exp}}/\langle I_0\rangle$ and modeled $I_{1,\text{theo}}/\langle I_0\rangle$ linear intensity, respectively, corresponding to the line-cuts shown in (b). (e.) The second-order intensity contribution $I_2(x = 0\,\text{mm}, y, t = 0)$ extracted from the schlieren data in (a) and two stroboscopic measurements at $\omega t = \pi/2$ and $3\pi/2$.

3.3. Acoustic levitator

The acoustic fields giving rise to the levitation traps are created using a double-sided phased array of transducers (PAT)-based levitator [29]. The transducers (Murata MA40S4S) in the two PATs are arranged in 8 × 8 planar grids with a spacing (center-to-center) of 10 mm along the x and z-axis, resulting in a total array length and width of 80 mm, and an inter-array distance of 92 mm. Each transducer is driven by an individually controllable 39.8 kHz sinusoidal signal with $V_p = 16\,\text{V}$. The signals are generated by a FPGA-based system-on-module combined with analogue low-pass filters and power amplifiers [30].

In the following, we discuss the modeling of the pressure field generated by the PATs of the levitator. Each transducer s generates a harmonic pressure field $p_s(\mathbf{r}, t) = \Re\left(p_s(\mathbf{r})\exp(i\omega t)\right)$. Its spatial dependence $p_s(\mathbf{r})$ as function of position vector $\mathbf{r}$ can be expressed as

$$p_s(\mathbf{r}) = P_0 D_s(\mathbf{r}) \frac{\exp(i\left(k|\mathbf{r} - \mathbf{r}_s|\right))}{|\mathbf{r} - \mathbf{r}_s|} a_t \exp(-i\varphi_s), \tag{5}$$

where P_0 (= 2.72 Pa[6]) corresponds to the reference pressure, $D_s(\mathbf{r})$ denotes a far-field directivity function, $k = 2\pi/\lambda$ is the wave vector with λ being the wavelength of the sound generated by the transducer, $\mathbf{r}_s$ is the position vector of transducer s (relative to the center of the levitator), a_t is the transducer's pressure amplitude relative to a reference pressure P_0 and φ_s is an additional phase offset relative to a reference phase. In this work, a_t was set identical for all transducers in the PATs while the phase delay φ_s of each transducer is independently adjusted to optimize the pressure field to effectively create the focal points/levitation traps at desired positions [6].

The directivity function is approximated employing a single frequency baffled piston model,

$$D_s(\mathbf{r}) = 2\frac{J_1\left(ka\sin(\vartheta_s(\mathbf{r}))\right)}{ka\sin(\vartheta_s(\mathbf{r}))} \tag{6}$$

with $J_1(\cdot)$ the Bessel function of first order and first kind, $\vartheta_s(\mathbf{r})$ the angle between transducer normal and spatial point $\mathbf{r}$, and a (= 4.5 mm) the effective radius of the transducers [6]. The total pressure field in the levitator is then given by the superposition of the $N = 128$ single transducers. The averaged pressure p_{2D} generated by the PATs, that is probed by schlieren according to Eq. (1), can be calculated by integrating the pressure field over the length of the acoustic levitator in the direction of the optical axis ($L = 8\,\text{cm}$),

$$p_{2D}(x, y) = \frac{1}{L}\sum_{s=1}^{N}\int_0^L p_s(x, y, z')\mathrm{d}z'. \tag{7}$$

For a certain configuration of the PATs, we employ numerical integration to obtain the modeled p_{2D} from Eq. (7).

4. Experimental results and analysis of phase-shifted stroboscopic schlieren technique

In Fig. 2, the application of the phase-shifted stroboscopic extraction method presented in Section 3.1 is demonstrated for the acoustic field with a focal point at the center of the levitator, $\mathbf{r} = (0, 0, 0)$. The starting point of our analysis is the measurement of the two stroboscopic schlieren images at times $t = 0$ (see Fig. 1(d)) and $t = \pi/\omega$. Fig. 2(a) shows line-cuts of the schlieren images along the y-axis through the center of the focal point at $x = 0\,\text{mm}$. They are normalized to the average background illumination $\langle I_0\rangle$ which is measured when the pressure field is switched off, with the black and gray curves indicating the intensity obtained for $\omega t = 0$ and π, respectively. When comparing the two intensity curves, we observe the expected phase shift of π between the two measurements. We find that the intensity peaks are sharper than the valleys and the points where the black and gray curves cross, marked by the dotted line in Fig. 2(a), are shifted towards lower intensity values near the levitator center. These observations are indicative of nonlinear effects that affect the schlieren images.

To determine the linear contribution I_1, we apply the method described in Section 3.1 and Eq. (4). Subtracting the two stroboscopic intensity measurements in Fig. 2(a) from each other, i.e. $I_{1,\text{exp}}(y)/\langle I_0\rangle = \frac{1}{2\langle I_0\rangle}(I(x = 0, y, t = 0) - I(x = 0, y, t = \pi/\omega))$, results in the 'exp.' (experimental) I_1 curve shown in Fig. 2(b). The background is indiscernible and the intensity curve has become symmetric around the $I_1 = 0$ line. For comparison, the 'theo' (theoretical) intensity curve, obtained from the modeled pressure field by $I_{1,\text{theo}}(x, y)/\langle I_0\rangle = c_1 2L\partial_y p_{2D}(x, y)$ at $x = 0\,\text{mm}$ is plotted as a dotted line in Fig. 2(b). To obtain the modeled pressure field, we use the procedure described in Section 3.3 and Eq. (7), where p_{2D} relates to the integrated pressure field along the optical axis over the length of the levitator $L = 8\,\text{cm}$. The constant c_1 represents the transduction factor by which the schlieren setup converts

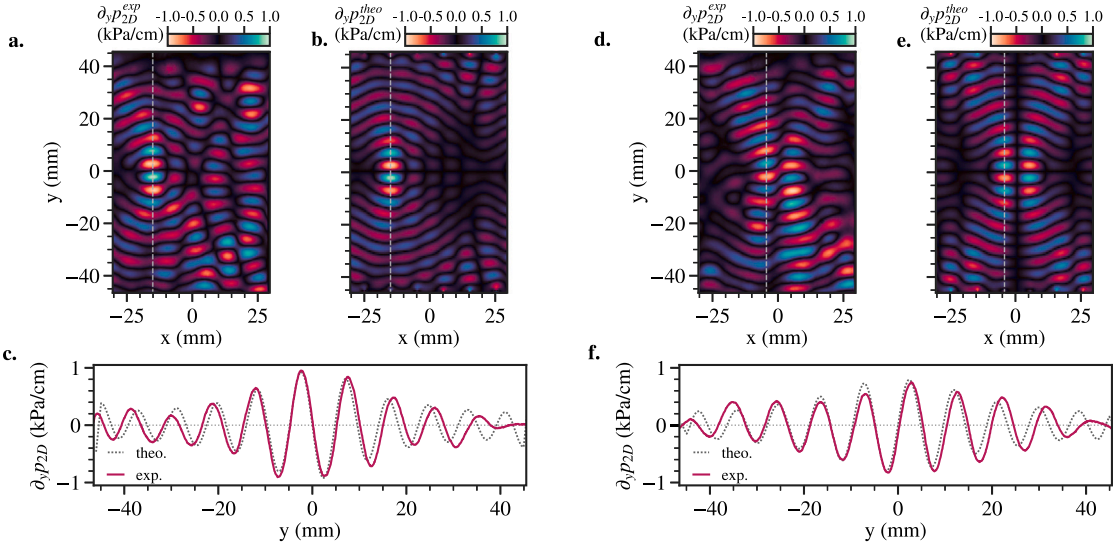

Fig. 3. Phase-shifted stroboscopic analysis applied to varying acoustic fields. The extracted intensity using the phase-shifted stroboscopic method for a shifted focus point created in $\mathbf{r} = (-15\,\mathrm{mm}, 0, 0)$ and for a twin-trap in $\mathbf{r} = (0, 0, 0)$ are shown in (a.) and (d.) with their corresponding modeled pressure y-derivatives given in (b.) and (e.). The line cuts marked by the gray lines in the experimental and modeled fields of the shifted focus point and twin trap are plotted in (c.) and (f.), respectively.

a pressure gradient $\partial_y p_{2\mathrm{D}}$ to a normalized linear optical intensity I_1. The value of c_1 is determined from the $x = 0\,\mathrm{mm}$ line-cut such that the peak–valley distances for $I_{1,\mathrm{exp}}$ and $I_{1,\mathrm{theo}}$ are equal near $\mathbf{r} = (0, 0, 0)$ by evaluating the following equation over the range $-\frac{\lambda}{2} \leq y \leq \frac{\lambda}{2}$,

$$c_1 = \frac{1}{2L\langle I_0\rangle} \frac{\max\left(I_{1,\mathrm{exp}}(y)\right) - \min\left(I_{1,\mathrm{exp}}(y)\right)}{\max\left(\partial_y p_{2\mathrm{D}}(y)\right) - \min\left(\partial_y p_{2\mathrm{D}}(y)\right)}, \tag{8}$$

resulting in $c_1 = 8.9 \cdot 10^{-5}\,\mathrm{Pa}^{-1}$. We find a good agreement between the experimentally determined and modeled I_1 in the vicinity of the focal point. In the off-center regions the intensity amplitudes seem to be reasonable described by the theory as well, however, we observe a slight de-phasing of the measured pressure field gradient. A similar observation can be made for the 2D-images corresponding to the line-cuts in Fig. 2(b) of the linearized intensity $I_{1,\mathrm{exp}}/\langle I_0\rangle$, obtained from the schlieren images, shown in Fig. 2(c) and the modeled intensity $I_{1,\mathrm{theo}}/\langle I_0\rangle$ shown in Fig. 2(d); we find a good agreement over the whole image with slight deviations in the off-center areas. The overall reasonable match in amplitudes indicates that the transduction factor of the schlieren setup is roughly constant throughout the field of view.

It is worth noting that by using a similar approach as that used for extracting I_1, the higher order term I_2 can also be estimated from the schlieren images. According to Eq. (3), we find that

$$2I_2(x, y, t = 0) = I(x, y, t = 0) + I\left(x, y, t = \frac{\pi}{\omega}\right) - \left[I\left(x, y, t = \frac{\pi}{2\omega}\right) + I\left(x, y, t = \frac{3\pi}{2\omega}\right)\right]. \tag{9}$$

We use this equation to generate the line-cut of the estimated I_2 in Fig. 2(e) from the schlieren data in Fig. 2(a) and two additional stroboscopic schlieren measurements taken at $\omega t = \pi/2$ and $3\pi/2$. As expected, the wavelength is halved compared to $I_{1,\mathrm{exp}}$ and the whole curve is shifted below zero. This fits well with the observed downward shift of the crossings in Fig. 2(a). It can also be seen from Fig. 2(e) that the contribution of the nonlinear term I_2 to the schlieren image is substantial, and has a non-negligible amplitude compared to that of I_1 shown in Fig. 2(b).

To further explore the phase-shifted stroboscopic schlieren extraction method for determining the pressure gradient, and to test whether the value of the transduction factor c_1 remains a roughly constant property of the schlieren setup, we apply the method to two other acoustic fields.

For the first field (Fig. 3(a)–(c)), we generate an acoustic focal point 15 mm left from the center of the levitator at $\mathbf{r} = (-15\,\mathrm{mm}, 0, 0)$. From our measurements we obtain a peak-to-peak ratio of $c_1 = 6.9 \cdot 10^{-5}\,\mathrm{Pa}^{-1}$. Using this transduction factor, we find the estimated pressure gradient $\partial_y p_{2\mathrm{D}}^{exp}$ shown in Fig. 3(a); a high amplitude standing wave at $x = -15\,\mathrm{mm}$ is clearly visible and we observe again a good agreement with the modeled pressure gradient $\partial_y p_{2\mathrm{D}}^{theo}$ as shown in Fig. 3(b). This agreement is validated by the comparison of the line-cuts at $x = -15\,\mathrm{mm}$ of the experimental and theoretical pressure gradient in Fig. 3(c) (line-cut position is marked by the gray dashed lines in Figs. 3(a) and (b)). When shifting away from the focal point, we do find, however, slightly higher intensity values than expected from the theory.

In the second acoustic field (Fig. 3(d)–(f)) we create a twin-trap at $\mathbf{r} = (0, 0, 0)$. The twin trap is generated as described in Ref. [7] where the transducers are optimized to generate a focal point at $\mathbf{r} = (0, 0, 0)$, then an additional phase of π is added to every transducer for which the transducer's position satisfies $x_s < 0\,\mathrm{mm}$. The extracted image representing the estimated $\partial_y p_{2\mathrm{D}}^{exp}$ is shown in Fig. 3(d). The corresponding theoretical spatial derivative of the acoustic field is given in Fig. 3(e). The line-cuts of the schlieren image and the modeled derivative are shown in Fig. 3(f) and we observe similar trends as with the previously analyzed fields; a general agreement with deviations in the low pressure regions. The line-cut in Fig. 3(f) is taken at $x = -4.7\,\mathrm{mm}$, corresponding to the location where the amplitude has the highest value. An interesting feature of this particular acoustic field is the expected symmetry around the nodal-line $x = 0\,\mathrm{mm}$, which allows to determine c_1 at the two equivalent positions of $x_\pm = \pm 4.7\,\mathrm{mm}$. As expected from Eq. (8), the peak-to-peak ratios result in similar values for the transduction factor at both sides of the symmetry axis: $c_1 = 7.3 \cdot 10^{-5}\,\mathrm{Pa}^{-1}$ for negative $x_- < 0\,\mathrm{mm}$ and $c_1 = 7.0 \cdot 10^{-5}\,\mathrm{Pa}^{-1}$ for positive $x_+ > 0\,\mathrm{mm}$.

In the theoretical analysis it was assumed that the stroboscopic illumination pulses are very short compared to the period of the ultrasound. However, experimentally it is desirable to work with longer pulses because they result in a brighter image and decreased image noise on the camera. It is therefore of interest to see whether good results can still be obtained by longer duty cycles of the LED illumination. Here, the duty cycle is defined as the percentage of the time the LED is on (t_{on}/T).

In Fig. 4(a), (b) we extract I_1 at the central focal point for varying LED duty cycles. It can be seen in Fig. 4(a) that up to a duty cycle of 40% the shape of the schlieren intensity curve is roughly constant. A comparison between these duty cycle dependent intensity curves and the theoretical expectation is shown in supplemental Sec. 2 with the

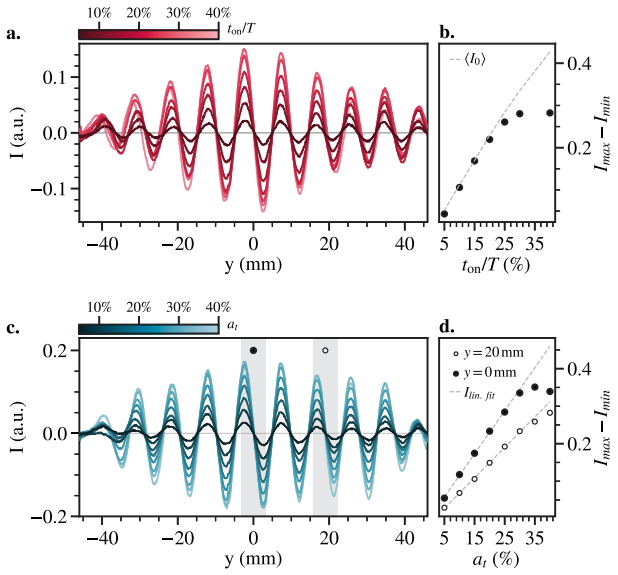

Fig. 4. Influence of the LED duty cycle and relative transducer amplitude on the extracted intensity. Line-cuts through $x = 0$ mm of the focal point field are plotted for varying LED duty cycle t_{on}/T (a.) and relative transducer amplitude a_t(c.). The progression of the peak-to-peak value of the central extremums (marked by the filled data point) and of side extremums (marked by the empty data point) are shown in (b.) and (d.) for the changing LED duty cycle and transducer amplitude, respectively. In (b.), the gray dashed line represents the average intensity without the presence of a pressure field as function of the duty cycle.

corresponding plot shown in Fig. S2. However, as is clear from Fig. 4(b), the linear relation between duty cycle and I_1 breaks down above duty cycles larger than 20%. This deviation is attributed to the fact that the strobe pulse length becomes so large that the schlieren intensity $I(t)$ varies substantially during the pulse, and cannot be assumed to be representative of an instantaneous intensity anymore. Consequently, the LED duty cycle was set to $t_{on}/T = 20\%$ during the schlieren image acquisition of Figs. 2, 3 and 4(c).

A second critical parameter of the schlieren setup is the maximum resolvable pressure amplitude. The pressure amplitude generated by our levitator is controlled by the relative transducer amplitude (a_t) parameter, as given in Eq. (5). Fig. 4(c) shows the extracted I_1 line-cuts through the focal point at $x = 0$ mm for a_t values between $5 - 40\%$. The comparison between the theoretical intensity and the pressure dependent intensity line-cuts are provided in supplemental Sec. 2. We find that the shape of $I_1(y)$ is roughly identical for all a_t (see also supplemental Fig. S3). The extracted peak-to-peak values of the gray shaded areas at $x = 0$ mm and $x = 20$ mm are given by the filled and empty data points in Fig. 4(d), respectively. Here, we find that the peak-to-peak values at $x = 0$ mm display a linear increase up to $a_t \approx 25\%$ after which a saturation sets in for higher amplitudes. Contrary to the duty cycle dependency, however, this saturation point is not reached for the peak-to-peak values at $x \approx 20$ mm. We attribute this longer persistence of linear response, up to a larger value of a_t, to the lower pressure amplitude at $y = 20$ mm.

5. Discussion

Although schlieren has been widely applied for several centuries, the nonlinearities in the relation between schlieren intensity and refractive index gradient have received relatively little attention, specifically for acoustic levitation fields. In this article we show that second order nonlinearities can have a substantial effect on the schlieren image of ultrasound pressure fields, and present a methodology for eliminating these nonlinearities by making use of the time-harmonic variation of the pressure field. With a phase-shifted stroboscopic schlieren technique the linear schlieren intensity I_1 can be extracted from the pressure gradient using $I_1(x, y) = c_1 2L\langle I_0 \rangle \partial_y p_{2D}(x, y)$, where $\langle I_0 \rangle$ is the spatially averaged background intensity and L the integration length of the pressure field.

In order to determine the effectiveness of our method for eliminating the second-order intensity from the schlieren images, we compare the peak to peak amplitudes of the linear part I_{pp1} in Fig. 2(b) and of the nonlinear part I_{pp2} in Fig. 2(e) of the schlieren image. From that comparison we find that $I_{pp2}/I_{pp1} \approx 0.19$, indicating that the presented method for the presented acoustic levitation pressure field corrects errors of about 19% due to the higher order nonlinear terms, in addition to removing the constant background.

By comparing simulations of the pressure field to experimental schlieren images we have obtained estimates for c_1 that range between $6.9 \cdot 10^{-5}$ and $8.9 \cdot 10^{-5}$ Pa^{-1}. The close correspondence between these values shows that once an accurate calibration for a known pressure field has been performed, the value of c_1 can be used to quantitatively estimate unknown pressure fields. It was observed that near the edge of the levitator, differences between measured and modeled pressure fields increased, resulting in higher error margins. The observed deviations between the modeled and measured pressure fields could be caused by reflections of the ultrasound from the PATs and rigid levitator components. Furthermore, natural variation in properties and placement of the transducers that were not captured in the optimization procedure of the transducer phases may also lead to differences between applied and modeled pressure field. These sources of disturbance can furthermore lead to interfering pressure fields from the top and bottom array that will cause parasitic traveling sound waves to be generated that can distort the schlieren images. In general, a linear harmonic pressure field containing both standing and traveling waves might be described by

$$p_{2D}(x, y, t) = p_{2D,I}(x, y)\cos(\omega t) + p_{2D,Q}(x, y)\sin(\omega t) \tag{10}$$

where $p_{2D,I}(x, y)$ is the in-phase amplitude (with respect to the standing wave field) and $p_{2D,Q}(x, y)$ is the amplitude of the quadrature (i.e. 90° phase shifted) term. E.g. for a plane sound wave traveling in the positive x direction with wavenumber k we have $p_{2D}(x, y, t) = a_{2D}\cos(kx - \omega t)$ resulting in $p_{2D,I}(x, y) = a_{2D}\cos(kx)$ and $p_{2D,I}(x, y) = a_{2D}\sin(kx)$.

Essentially, the presence of traveling waves, in addition to standing waves, results in the emergence of the $p_{2D,Q}(x, y)$ term, whose linear component I_1 can be extracted in a similar way as that for the standing wave part $p_{2D,I}(x, y)$. However, to obtain both $p_{2D,I}(x, y)$ and $p_{2D,Q}(x, y)$ will require applying Eq. (4) twice, at moments t_1 and $t_1 \to t_1 + \pi/(2\omega)$ to obtain both $I_{1,I}$ and $I_{1,Q}$.

It is of interest to see whether the transduction factor c_1 can be estimated from the schlieren setup parameters. In the ray approximation, for non-coherent light, a refractive index gradient $\partial_y n = \partial n/\partial y$ results in an angular deflection [26] $\alpha = 2L\partial_y n \approx 2L\kappa\partial_y p$. Partial blocking of the deflected rays by the knife-edge converts these pressure induced deflection angles to intensity modulations, which in the linear regime can be approximated by $I = (dI/d\alpha)\alpha$. In the ray approximation we can assume that the maximal deflection angles for which the ray is still partly cut by the knife edge is given by $\pm\alpha_{max} \approx \pm R/2f$, translating to a maximal intensity amplitude of $2\langle I_0 \rangle$. The transduction factor then becomes $dI/d\alpha = 2f\langle I_0 \rangle/R$. Comparison with Eq. (1) results in an estimated $c_1 \approx 2f\kappa/R \approx 14.6 \cdot 10^{-5}$ Pa^{-1} (see supplemental Sec. 3). Although this value is somewhat higher than the experimentally obtained values for c_1, this model for incoherent light gives a rough first approximation. The exact value for c_1 may moreover depend on schlieren system specific parameters such as the exact knife-edge position in the y-direction and camera sensitivity. To obtain c_1, we recommend measuring a known linear refractive index gradient with the schlieren setup, e.g. a thin lens [26]. This allows to determine the calibration factor between the intensity and the refractive index

gradient $\partial_y n$ from which the transduction factor c_1 can be determined using that in the linear case $n \approx 1 + \kappa p$ (see Section 2).

Although we do get $\partial_y p_{2D}$ from the presented method, this does not provide us with the full 3D pressure field. To obtain p_{2D} we can numerically integrate $\partial_y p_{2D}$ in the y-direction. To obtain the 3D field requires tomography in which multiple schlieren images, at different angles are used [31]. Tomography might be combined with the presented stroboscopic technique for eliminating nonlinearities.

An important final remaining question is whether we can identify the mechanism that generates the nonlinearities. Probably either nonlinear acoustic effects, or nonlinear effects in the schlieren mapping $\mathcal{F} : p_{2D}(x, y) \rightarrow I(x_s, y_s)$ play a role. However, a full discussion of this topic is out of the scope of this paper, and we are preparing a manuscript to discuss this question in more detail and analyze the origin and relevance of nonlinearities in schlieren.

6. Conclusion

Schlieren imaging is a powerful technique for visualizing pressure fields in acoustic levitators. However, as we have shown, nonlinear effects can distort the images, which complicates using them for quantitative analysis. Here, a phase-shifted stroboscopic method for extracting the linear part of the schlieren image was proposed, and it was shown to agree well to modeled pressure fields, providing evidence that the method can contribute to a better quantitative analysis of schlieren images once the transduction factor c_1 is properly calibrated. The proposed approach allows for better quantitative analysis of harmonically varying refractive index variations, which is especially relevant for optimizing pressure fields in ultrasonic transducer arrays for acoustic levitation applications.

CRediT authorship contribution statement

Frederike S.L. Wörtche: Methodology, Formal analysis, Writing – original draft, Conceptualization, Visualization, Investigation, Data curation. **Fabian Maucher:** Writing – original draft, Conceptualization, Writing – review & editing, Formal analysis. **Martijn Mooiweer:** Conceptualization, Resources. **Gerard J. Verbiest:** Supervision, Conceptualization, Writing – review & editing. **Peter G. Steeneken:** Funding acquisition, Writing – review & editing, Supervision, Conceptualization, Writing – original draft, Formal analysis.

Declaration of competing interest

The authors declare the following financial interests/personal relationships which may be considered as potential competing interests: Frederike S. L. Wortche reports financial support was provided by ITEC B.V. Frederike S. L. Wortche reports financial support was provided by Netherlands Enterprise Agency (RVO). Fabian Maucher reports financial support was provided by ITEC B.V. Fabian Maucher reports financial support was provided by Netherlands Enterprise Agency (RVO). Martijn Mooiweer reports financial support was provided by ITEC B.V. Martijn Mooiweer reports financial support was provided by Netherlands Enterprise Agency (RVO). Gerard J. Verbiest reports financial support was provided by ITEC B.V. Gerard J. Verbiest reports financial support was provided by Netherlands Enterprise Agency (RVO). Peter G. Steeneken reports financial support was provided by ITEC B.V. Peter. G. Steeneken reports financial support was provided by Netherlands Enterprise Agency (RVO). If there are other authors, they declare that they have no known competing financial interests or personal relationships that could have appeared to influence the work reported in this paper.

Acknowledgments

The authors thank J. Wesselingh, J. Stokkermans, G. van der Veen, H. van der Linden and R.H. Guis for their support. This work was financed by ITEC B.V. and co-financed by the Netherlands Enterprise Agency (RVO).

Appendix A. Supplementary data

Supplementary material related to this article can be found online at https://doi.org/10.1016/j.ultras.2025.107743.

Data availability

Data will be made available on request.

References

[1] A. Kundt, Ueber eine neue art akustischer staubfiguren und über die anwendung derselben zur bestimmung der schallgeschwindigkeit in festen körpern und gasen, Ann. Phys., Lpz. 203 (4) (1866) 497–523, http://dx.doi.org/10.1002/andp.18662030402.

[2] P. Gor'kov, On the forces acting on a small particle in an acoustical field in an ideal fluid, Dokl. Akad. Nauk SSSR 140 (1961) 88.

[3] H. Bruus, Acoustofluidics 7: The acoustic radiation force on small particles, Lab Chip 12 (2012) 1014–1021, http://dx.doi.org/10.1039/C2LC21068A.

[4] Y. Ochiai, T. Hoshi, J. Rekimoto, Pixie dust: graphics generated by levitated and animated objects in computational acoustic-potential field, ACM Trans. Graph. 33 (4) (2014) 1–13, http://dx.doi.org/10.1145/2601097.2601118.

[5] T. Omirou, A. Marzo, S.A. Seah, S. Subramanian, Levipath: Modular acoustic levitation for 3d path visualisations, in: Proceedings of the 33rd Annual ACM Conference on Human Factors in Computing Systems, CHI '15, Association for Computing Machinery, New York, NY, USA, 2015, pp. 309–312, http://dx.doi.org/10.1145/2702123.2702333.

[6] A. Marzo, B.W. Drinkwater, Holographic acoustic tweezers, Proc. Natl. Acad. Sci. 116 (1) (2019) 84–89, http://dx.doi.org/10.1073/pnas.1813047115.

[7] A. Marzo, S.A. Seah, B.W. Drinkwater, D.R. Sahoo, B. Long, S. Subramanian, Holographic acoustic elements for manipulation of levitated objects, Nat. Commun. 6 (1) (2015) 8661, http://dx.doi.org/10.1038/ncomms9661.

[8] R.H. Morris, E.R. Dye, P. Docker, M.I. Newton, Beyond the langevin horn: Transducer arrays for the acoustic levitation of liquid drops, Phys. Fluids 31 (10) (2019) 101301, http://dx.doi.org/10.1063/1.5117335.

[9] V. Vandaele, P. Lambert, A. Delchambre, Non-contact handling in microassembly: Acoustical levitation, Precis. Eng. 29 (4) (2005) 491–505, http://dx.doi.org/10.1016/j.precisioneng.2005.03.003.

[10] D. Foresti, M. Nabavi, M. Klingauf, A. Ferrari, D. Poulikakos, Acoustophoretic contactless transport and handling of matter in air, Proc. Natl. Acad. Sci. 110 (31) (2013) 12549–12554, http://dx.doi.org/10.1073/pnas.1301860110.

[11] A. Watanabe, K. Hasegawa, Y. Abe, Contactless fluid manipulation in air: Droplet coalescence and active mixing by acoustic levitation, Sci. Rep. 8 (1) (2018) 10221, http://dx.doi.org/10.1038/s41598-018-28451-5.

[12] J.W.E. Drewitt, B. Emmens, Z.-H. Kong, B.W. Drinkwater, A.C. Barnes, Mightylev: An acoustic levitator for high-temperature containerless processing of medium- to high-density materials, Rev. Sci. Instrum. 95 (10) (2024) 103903, http://dx.doi.org/10.1063/5.0221899.

[13] T. Fushimi, A. Marzo, B.W. Drinkwater, T.L. Hill, Acoustophoretic volumetric displays using a fast-moving levitated particle, Appl. Phys. Lett. 115 (6) (2019) 064101, http://dx.doi.org/10.1063/1.5113467.

[14] R. Hirayama, D. Martinez Plasencia, N. Masuda, S. Subramanian, A volumetric display for visual, tactile and audio presentation using acoustic trapping, Nature 575 (7782) (2019) 320–323, http://dx.doi.org/10.1038/s41586-019-1739-5.

[15] P. Helander, T. Puranen, A. Meriläinen, G. Maconi, A. Penttilä, M. Gritsevich, I. Kassamakov, A. Salmi, K. Muinonen, E. Haeggström, Omnidirectional microscopy by ultrasonic sample control, Appl. Phys. Lett. 116 (19) (2020) 194101, http://dx.doi.org/10.1063/5.0002602.

[16] I. Ezcurdia, R. Morales, M.A.B. Andrade, A. Marzo, Leviprint: Contactless fabrication using full acoustic trapping of elongated parts, in: ACM SIGGRAPH 2022 Conference Proceedings, SIGGRAPH '22, Association for Computing Machinery, New York, NY, USA, 2022, http://dx.doi.org/10.1145/3528233.3530752.

[17] A. Stindt, M.A. Andrade, M. Albrecht, J. Adamowski, U. Panne, J. Riedel, Experimental and numerical characterization of the sound pressure in standing wave acoustic levitators, Rev. Sci. Instrum. 85 (1) (2014) 015110, http://dx.doi.org/10.1063/1.4861197.

[18] E. Tenenbaum, E. Baruch, A. Dolev, I. Bucher, Laser doppler vibrometer measurements of the 3d pressure field for the estimation of the radiation force produced by an acoustic standing-wave levitator, Sensors Actuators A 374 (2024) 115505, http://dx.doi.org/10.1016/j.sna.2024.115505.

[19] D.P. Jackson, M.-H. Chang, Acoustic levitation and the acoustic radiation force, Am. J. Phys. 89 (4) (2021) 383–392, http://dx.doi.org/10.1119/10.0002764.

[20] V. Contreras, K. Volke-Sepúlveda, Enhanced standing-wave acoustic levitation using high-order transverse modes in phased array ultrasonic cavities, Ultrasonics 138 (2024) 107230, http://dx.doi.org/10.1016/j.ultras.2023.107230.

[21] H. Reynoso-de la Cruz, E. Hernández-Campos, E. Ortiz-Ricardo, A. Martínez-Borquez, I. Rosas-Román, V. Contreras, G. Ramos-Ortiz, B. Mendoza-Santoyo, C.I. Zurita-Lopez, R. Castro-Beltrán, Acoustically levitated whispering-gallery mode microlasers, Opt. Laser Technol. 171 (2024) 110352, http://dx.doi.org/10.1016/j.optlastec.2023.110352.

[22] C.H. Hsu, H.Y. Lin, A. Agarwal, I. Davis, K.P. Nolan, K.B. Lua, The performance of an acoustic levitator, J. Phys.: Conf. Ser. 1509 (1) (2020) 012027, http://dx.doi.org/10.1088/1742-6596/1509/1/012027.

[23] V. Contreras, A. Marzo, Adjusting single-axis acoustic levitators in real time using rainbow schlieren deflectometry, Rev. Sci. Instrum. 92 (1) (2021) 015107, http://dx.doi.org/10.1063/5.0013347.

[24] J.F. Pazos Ospina, V. Contreras, J. Estrada-Morales, D. Baresch, J.L. Ealo, K. Volke-Sepúlveda, Particle-size effect in airborne standing-wave acoustic levitation: Trapping particles at pressure antinodes, Phys. Rev. Appl. 18 (2022) 034026, http://dx.doi.org/10.1103/PhysRevApplied.18.034026.

[25] W. Rueckner, J. Peidle, A. Crockett, D. Davis, Particle size effects on stable levitation positions in acoustic standing waves, J. Acoust. Soc. Am. 154 (2) (2023) 1339–1346, http://dx.doi.org/10.1121/10.0020730.

[26] G.S. Settles, Schlieren and Shadowgraph Techniques, Springer Berlin Heidelberg, 2001, http://dx.doi.org/10.1007/978-3-642-56640-0.

[27] J.W. Goodman, Introduction to Fourier Optics, third ed., Roberts and Co., 2005.

[28] Y. Zhao, S. Yi, L. Tian, L. He, Z. Cheng, An experimental study of aero-optical aberration and dithering of supersonic mixing layer via bos, Sci. China Phys. Mech. Astron. 53 (2010) 81–94, http://dx.doi.org/10.1007/s11433-010-0111-4.

[29] Y. Ochiai, T. Hoshi, J. Rekimoto, Three-dimensional mid-air acoustic manipulation by ultrasonic phased arrays, PLoS One 9 (5) (2014) 1–5, http://dx.doi.org/10.1371/journal.pone.0097590.

[30] V. Bos, J. Wesselingh, G.J. Verbiest, P.G. Steeneken, Active damping for acoustic levitation in air, AIP Adv. 14 (9) (2024) 095009, http://dx.doi.org/10.1063/5.0210800.

[31] L. Bo, H. Cai, Y. Song, Y. Ji, Z. Li, A. He, Background-oriented schlieren tomography using gated recurrent unit, Opt. Express 31 (23) (2023) 39182–39200, http://dx.doi.org/10.1364/OE.505992.